Observations of near-surface fog at the Phoenix Mars landing site

John E. Moores,[1] Léonce Komguem,[1] James A. Whiteway,[1] Mark T. Lemmon,[2] Cameron Dickinson,[3] and Frank Daerden[4]

Received 26 November 2010; revised 5 January 2011; accepted 10 January 2011; published 25 February 2011.

[1] The Surface Stereo Imager (SSI) on the Phoenix Mars Lander was able to complement the operations of the LIDAR on four occasions during the mission by observing the laser beam while the LIDAR laser was transmitting. These SSI observations permitted measurement of the scatter from atmospheric aerosols below 200 m where the LIDAR emitter and receiver do not overlap fully. The observed laser scattering was used to estimate the ice-water content (IWC) of near surface fog. Values of IWC up to 1.7 ± 1.0 mg m^{-3} were observed. Compared to air aloft, fog formation was inhibited near the surface which had accumulated at least 30 ± 24 mg m^{-2} (0.030 pr-μm) on sol 113. Microphysical modeling shows that when precipitation is included, up to 0.48 pr-μm of water may be present on the surface at the time of measurement. Integrated over the entire night, this represents up to 2.5 pr-μm of water taken up diurnally by the surface, or 6% of the total water column. **Citation:** Moores, J. E., L. Komguem, J. A. Whiteway, M. T. Lemmon, C. Dickinson, and F. Daerden (2011), Observations of near-surface fog at the Phoenix Mars landing site, *Geophys. Res. Lett.*, *38*, L04203, doi:10.1029/2010GL046315.

1. Introduction

[2] The LIDAR instrument [*Whiteway et al.*, 2008] conducted measurements of dust and cloud within the Planetary Boundary Layer (PBL) of Mars over the course of the Phoenix Lander Mission [*Smith et al.*, 2009]. The instrument observed clouds in the upper PBL and water-ice fog near the surface in which particles grew sufficiently large to precipitate as evidenced by fall streaks [*Whiteway et al.*, 2009]. This precipitation provides a mechanism for water vapor mixed up to the top of the PBL during the day to return towards the surface at night.

[3] Retrieval of atmospheric optical characteristics from the LIDAR measurements were not possible below 200 m due to the transmitter-receiver overlap geometry. However, it is possible to determine the altitude distribution of water-ice particles close to the surface by using the LIDAR together with the Surface Stereo Imager (SSI). By imaging the path of the LIDAR beam with the SSI while the laser is transmitting, the particle scattering can be determined and from this measurement, the Ice-Water Content (IWC) of the near surface fog may be estimated. The presence of near surface water-ice fogs has previously been inferred from observations [i.e., *Hart and Jakosky*, 1986] and is predicted to form in numerical models [e.g., *Daerden et al.*, 2010] over a broad range of season and geographical extent. This letter will describe the first observations of the vertical profile of water-ice density within such fogs near the surface of Mars.

2. Measurements and Analysis

[4] There are four instances during the mission where the SSI was used to image the illuminated LIDAR beam at night. These were mission sol 61, between 02:45 and 02:53 Local True Solar Time (LTST) (L_S = 104.2°), sol 64 between 23:04 and 23:12 LTST (L_S = 106.0°), sol 82 between 00:50 and 00:56 LTST (L_S = 114.0°) and sol 113 between 23:39 and 23:51 LTST (L_S = 129.4°). In each case, the RB (R11) filter of the SSI, centered at 533nm with a bandwidth of 20.87nm, was employed to image the beam. A series of 10 images were captured over several minutes and averaged to even out the individual bright glints from ice crystals seen in the lower part of the beam. The camera was nominally centered at 83.9° upwards with respect to the site frame and a 256 × 1024 pixel subframe was used for all observations except on sol 61 when a full 1024 × 1024 frame was used. This orientation meant that the height of the beam on the frame was typically 965 pixels. See *Lemmon et al.* [2008], *Smith et al.* [2007] and *Moores et al.* [2010] for a description of the SSI instrument and geometry for atmospheric measurements.

[5] To extract the beam, a 75-pixel wide strip centered on the brightest part of the beam was removed and divided into three 25-pixel sections. The two side sections each provide a measure of background illumination at each level of the beam which were subtracted from the central section. This gives a spectral radiance value, $L_\lambda(El, Az)$, at each pixel in the central section due only to backscatter from the laser beam. *El* and *Az* are the corresponding elevation and azimuth angle for each pixel, respectively. Knowledge of the horizontal separation of the LIDAR laser and the SSI, 0.356 m, allows the elevation angle of each pixel to be mapped to a height, *z*, of the patch of sky illuminated by the laser beam. The error in the height derived in this way is made up of ±2 pixels based on the SSI pointing and up to ±10 pixels based on the pointing of the LIDAR, thus ±12 pixels (±2.8 mRad) will be used. The example of sol 113 shows that the error may be considerably less than this, as the illumination from the LIDAR beam returns to the level of background noise within 2 pixels of the SSI-derived zenith point.

[6] Using Mie-Debye theory and assuming that the optical depths of the fog between 0 and 200 m is small, the ice-water

[1]Centre for Research in Earth and Space Science, York University, Toronto, Ontario, Canada.
[2]Atmospheric Sciences Department Texas A&M University, College Station, Texas, USA.
[3]MacDonald Dettwiler and Associates Space Missions, Brampton, Ontario, Canada.
[4]Division of Planetary Aeronomy, Belgian Institute for Space Aeronomy, Brussels, Belgium.

0094-8276/11/2010GL046315

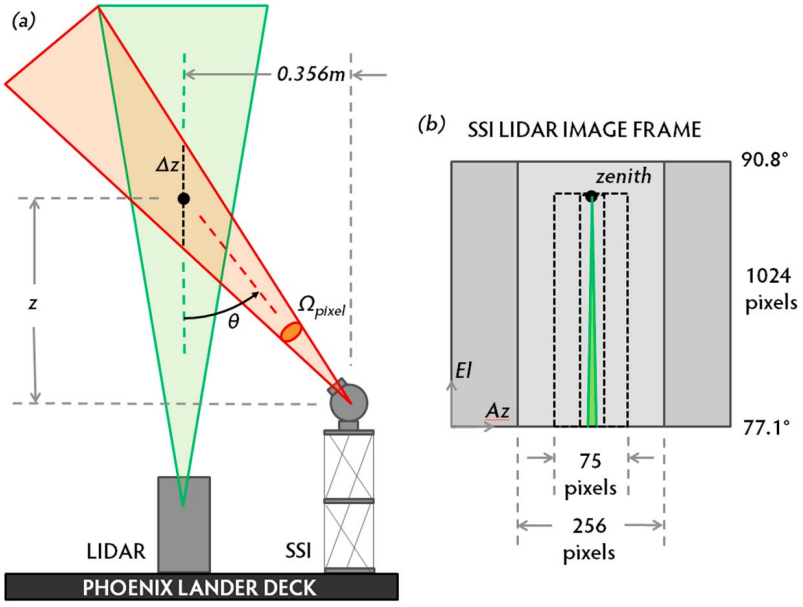

Figure 1. (a) An illustration of the geometrical parameters from equation (1) and (b) the extraction of the image of the LIDAR beam from the SSI frame with the boundaries of the two size 25-pixel wide background strips and central 25-pixel wide strip containing the LIDAR beam shown with dashed lines. Note that for clarity in Figure 1a the angle θ and the angular sizes of the LIDAR beam and an individual pixel are not shown to scale, similarly in Figure 1b the central 75 × 965 pixel extracted strip and 256 × 1024 pixel subframe are both shown larger than the horizontal scale of the 1024 × 1024 pixel SSI footprint.

content, *IWC*, of the scattering layer can be expressed in terms of the radiance observed at the SSI, L_λ,:

$$IWC = \sum_{Az} L_\lambda(z, Az) \frac{4\pi}{\phi(\theta)} \frac{z^2 \Omega_{pixel} \Delta\lambda}{P_{LIDAR} \cos^2\theta} \frac{1}{T^2(z)} \frac{2a\rho}{3\Delta z} \quad (1)$$

Here, is $\phi(\theta)$ the phase function at θ, the angle between the LIDAR beam and SSI pixel. P_{LIDAR} is the emitted LIDAR power of 0.040W at the source [*Whiteway et al.*, 2008] and $T(z)$ is the transmission of the LIDAR beam at height z. Δz is the height increment for each pixel, $\Delta\lambda$ is the bandwidth of the RB filter, 20.87nm, and Ω_{pixel} is the solid angle subtended by a single SSI pixel, 5.37×10^{-8} sr [*Smith et al.*, 2007]. The total radiation received by the SSI from a specific height is determined by summing the spectral radiance from each pixel in a row. Finally, a is the effective radius of the ice particles and ρ is their density. Note that these geometrical parameters are shown graphically in Figure 1.

[7] For the conditions present close to the surface at night, microphysical modeling [*Daerden et al.*, 2010] indicates that an effective radius of 20 μm is appropriate. In the angular range of interest, 167–180°, the value of $\phi(\theta)$ is not known for fog particles on Mars. However, as these clouds exist at similar water vapor pressure and temperature as terrestrial cirrus, an average value of 0.25 was used based upon field and laboratory observations of cirrus clouds [*Chepfer et al.*, 2002; *Baran*, 2009] over the entire angular range. It is of interest to note that the phase function curves provided by *Chepfer et al.* [2002] and *Baran* [2009] which are nearly constant between 167–180° also exhibit little or no enhancement at 22° and 46°; consistent with no SSI imagery showing discernible halos at these angles.

3. Results

[8] Figure 2 shows two observations with marginal detections of water-ice fogs during the earlier part of the mission while Figure 3 shows observations with unambiguous detections of water ice fogs during the latter part of the mission. The average spectral radiance has been plotted against pixel elevation angle in the site frame over the entire 1024 pixel height of the image in Figures 2b, 2e, 3b, and 3e. The corresponding value for *IWC* has been plotted against the height calculated from the geometry up to an altitude of 200 m above the lander in Figures 2c, 2f, 3c, and 3f.

[9] Table 1 shows values for the average *IWC* along with average and peak values of *IWC* and optical depth of the layers for all Sols on several ranges of interest. Sols 61 and 64 show a relatively constant distribution of *IWC* from the surface up to 200 m, whereas sols 82 and 113 show a peak between 40 and 50 m (+25/−12 m) and 50 and 60 m (+42/−17 m) respectively. The peak values for *IWC* at these altitudes are 1.7 ± 1.0 mg m^{-3} for sol 82 and 1.39 ± 0.47 mg m^{-3} for sol 113, comparable to values observed in the upper PBL using the LIDAR [*Whiteway et al.*, 2009]. In the layer closest to the surface, the lowest *IWC* value is on sol 113, with 0.51 ± 0.34 mg m^{-3} and the highest value seen on 61, with 1.3 ± 4.3 mg m^{-3}. This could represent an increase in the ability of the surface to remove water from the lower atmosphere as the season progresses and the ground cools. Optically, all water-ice layers seen are thin, with none having an optical depth of greater than 0.017.

4. Discussion and Conclusions

[10] Based on consistently produced PBL clouds after sol 70 as observed by the LIDAR [*Dickinson et al.*, 2010], radiative cooling to below the frost point at night is sufficient to explain the production of ice-water clouds within the PBL. Therefore formation of water-ice fogs near the surface is expected given that the frost point during the day is close to −60°C and near surface temperatures decrease to close to −90°C overnight [*Davy et al.*, 2010]. However, while this cooling is taking

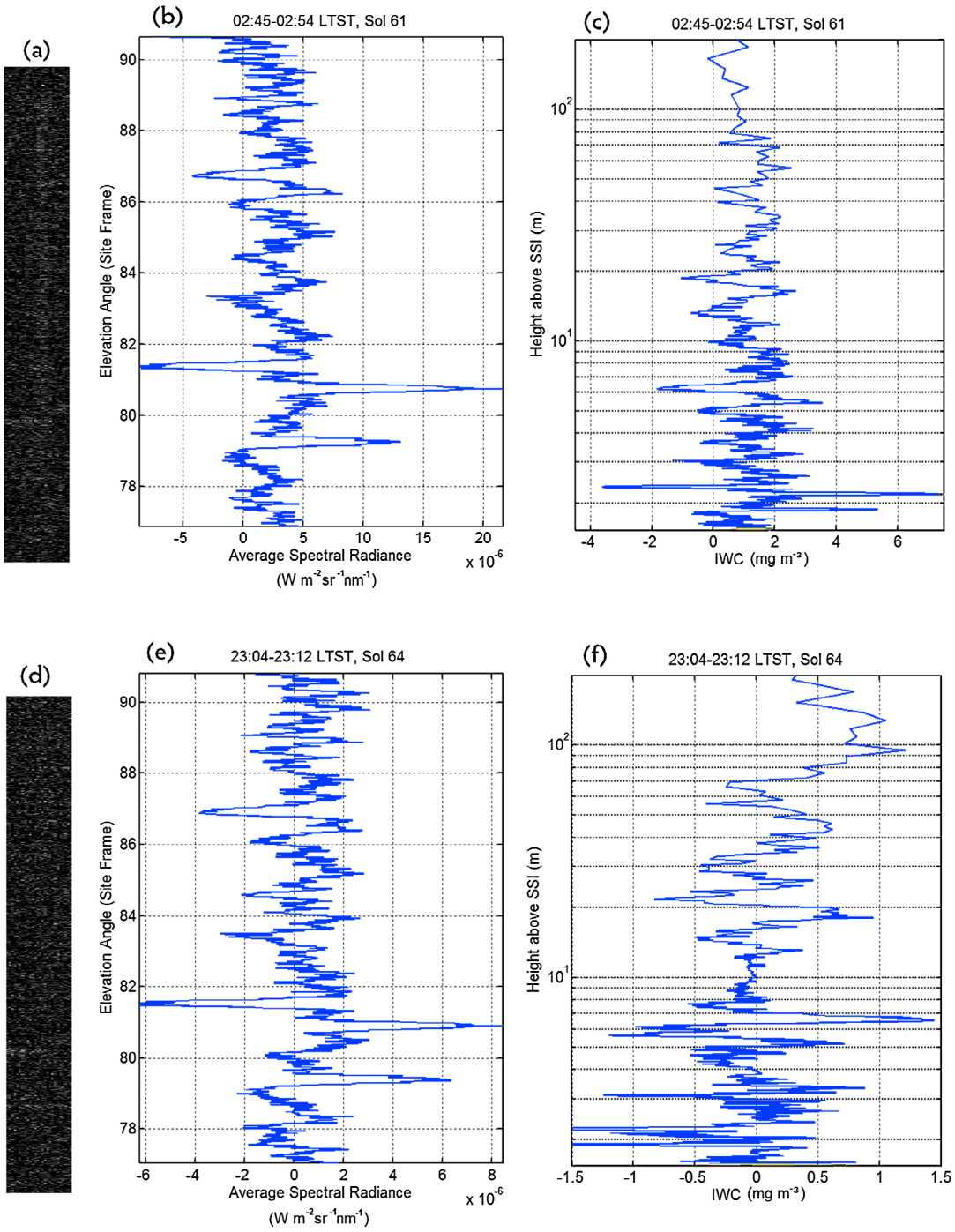

Figure 2. SSI images of the 25-pixel wide band centered on the LIDAR Beam on sols (a) 61 and (d) 64. (b and e) The corresponding average spectral radiance within the 25-pixel band is shown, as plotted against pixel elevation angle. (c and f) The calculated *IWC* distribution with height up to 200 m above the surface. The alternate axes on Figures 2c and 2f show the ice-water content. The sol 61 panels indicate a marginal detection while sol 64 shows no detection. *El* ± 2.8 mRad.

place, water vapor in direct contact with the ground is removed by direct deposition to the surface, physisorption and chemisorption on mineral grains [*Zent et al.*, 2010]. Thus, as mixing delivers more air to the ground, a region of reduced humidity (therefore less atmospheric IWC) is expected to form and increase its vertical extent with time.

[11] It is possible to examine these two competing effects using a simplistic version of the model described by *Davy* [2009] to determine at what times and at what heights water-ice fog would be expected to form. As boundary conditions, this diffusive model uses the TECP values for water vapor density near the surface [*Zent et al.*, 2010] as well as the MET temperature [*Davy et al.*, 2010] at 1 m above the lander deck. Above the surface, water vapor and thermal energy are permitted to mix, and the radiative effect of the cooling surface is taken into account. The atmosphere is assumed to be well mixed with constant potential temperature and water vapor density at 19:00 LMST, just prior

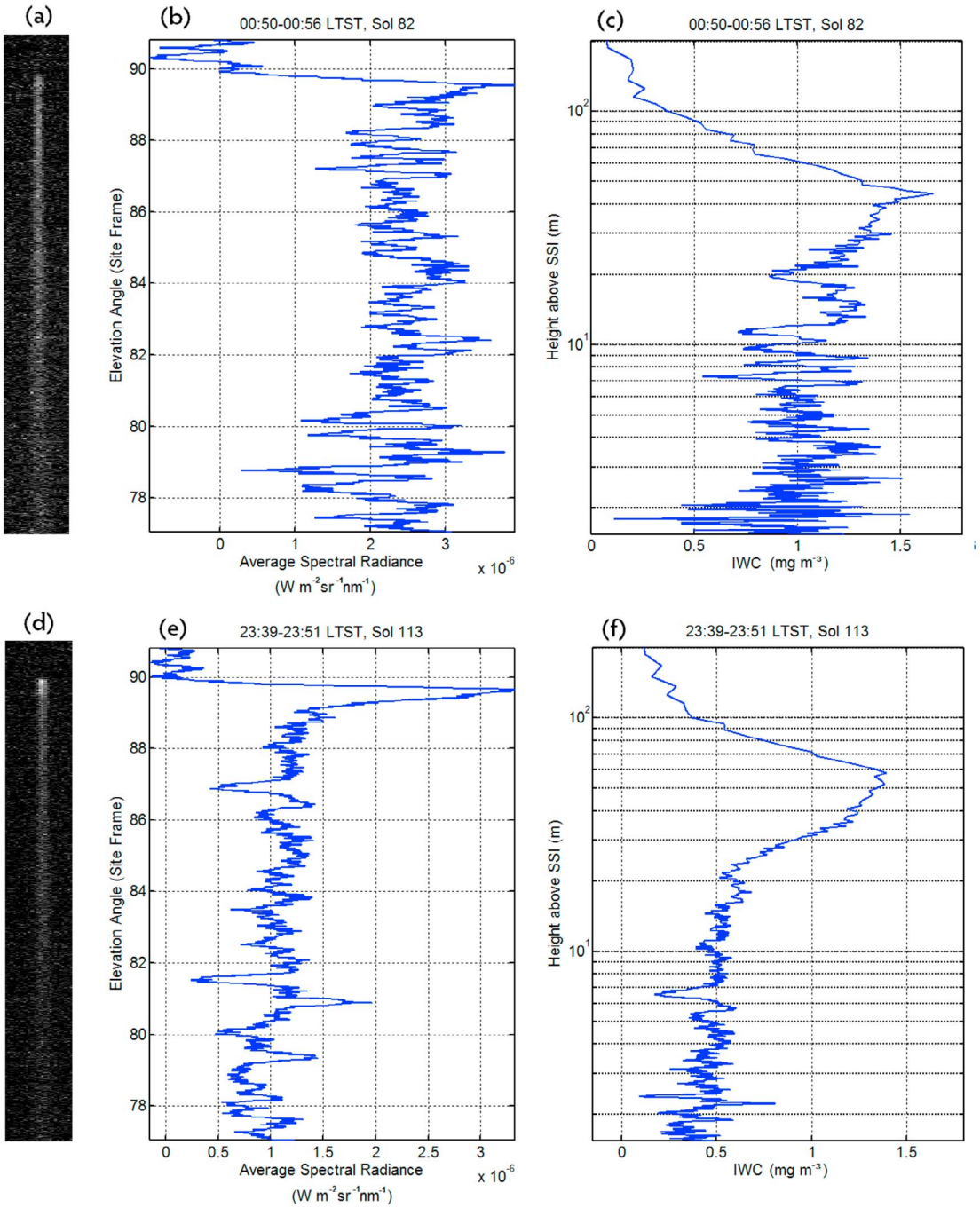

Figure 3. SSI images of the 25-pixel wide band centered on the LIDAR Beam on sols (a) 82 and (d) 113. (b and e) The corresponding average spectral radiance within the 25-pixel band is shown, as plotted against pixel elevation angle. (c and f) The calculated *IWC* distribution with height up to 200 m above the surface. The alternate axes on Figures 3c and 3f show the ice-water content. In contrast to Figure 2, scattering by the LIDAR beam is unambiguous and signal to noise ratios are improved. A layer is also observed between 40 and 50 m (+25/−12 m) on sol 82 and between 50 and 60 m (+42/−17 m) on sol 113. *El* ± 2.8 mRad.

to the average expected end of vigorous mixing within the PBL, as determined by examination of the MET temperature record described in [*Davy et al.*, 2010]. The diffusive model iterates the vapor density and temperature from this point. An eddy diffusivity of order 1 m^2s^{-1} was used, consistent with previous PBL modeling [*Davy*, 2009].

[12] The results of the diffusive model have been plotted as Figure 4. For these simulations there was no representation of microphysics in the diffusive model. The ice water content (IWC) of the cloud was determined as the amount of humidity in excess of saturation. It is assumed that the air remains saturated with respect to ice within the cloud. No water-ice aerosol would be expected to form on sol 64, as the atmosphere is too warm at the time of measurement. Sol 61 and sol 82 would both be expected to form water-ice particles with peak *IWC* in a layer near 70 m above the

Table 1. Average and Peak Values of IWC and Optical Depth

Sol	Range (m)	Average (*IWC*, mg m^{-3})	Peak (*IWC*, mg m^{-3})[a]	1-σ Error (*IWC*, mg m^{-3})	Total Column H_2O-ice (mg m^{-2})	Layer Optical Depth
61	0–80	1.3	-	4.3	96	0.010
61	0–200	0.90	-	4.3	166	0.017
64	0–100	0.42	-	1.7	36	0.004
64	0–200	0.50	-	1.7	89	0.009
82	0–20	1.1	-	0.76	20	0.002
82	20–60	1.3	1.7	1.0	52	0.005
82	0–200	0.52	1.7	0.77	113	0.011
113	0–20	0.51	-	0.34	9.4	0.001
113	20–90	1.01	1.4	0.47	72	0.007
113	0–200	0.57	1.4	0.37	116	0.012

[a]Peak values are applicable only on ranges which bracket a peak with S/N better than the 1-σ error.

ground. Ice may be distributed to lower levels by precipitation, which may account in part for the lack of a layer seen on sol 61. While these two observations would be expected to produce comparable amounts of ice, according to the diffusive model, the height of the sun, 8° above the horizon during the sol 61 observation, compared to 2° above the horizon during the sol 82 observation, means that more background light on sol 61 would make detection of this ice difficult. This is reflected in the large uncertainty given for *IWC* values on sol 61.

[13] Sol 113 contains the greatest amount of ice in the diffusive model simulations. At the time of observation the diffusive model predicts that the atmosphere will be supersaturated up to 100 m, with the thickest ice layer predicted to occur near 50 m of altitude, comparable to observations. Supersaturations within the lower 100 m of the column are predicted by the diffusive model to range up to almost 2.5 times saturation, or just over 1.8 mg m^{-3} of ice water content, assuming that all supersaturated water is consumed by deposition onto ice aerosols. This is comparable to the observed peak value of 1.39 ± 0.47 mg m^{-3} for sol 113. However, the observations on sols 61 and 82 show more water-ice within the lower 200 m of the atmosphere than would be expected from the diffusive model.

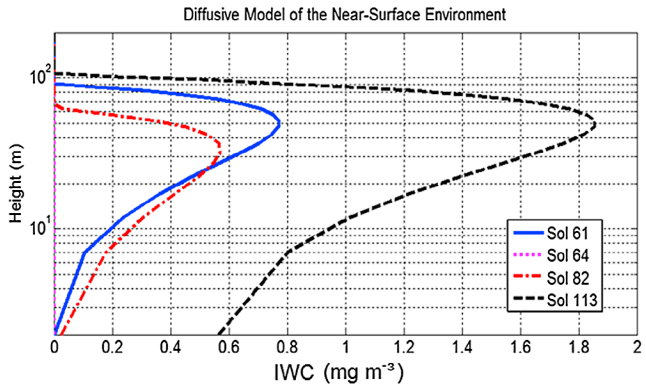

Figure 4. The results of a model run to determine the degree of supersaturation of air (with respect to water ice) with height above the ground. The MET temperature at 1 m above the deck and the average TECP profile were used to constrain the model. The measurements of sol 113 are expected to produce the thickest water-ice fog, whereas the measurements on sol 82 and 61 are expected to be similar. Sol 64 is not thought to have had the capacity to produce any fog due to undersaturated conditions.

[14] Temperatures below the expected peak in *IWC* will decrease towards the surface and will therefore be colder below 50 m than they are above. Thus, below the peak in *IWC*, condensation must be inhibited by a lack of water vapor. Since the mixing overnight is insufficient to transport this water vapor to higher altitude due to a significant surface-based temperature inversion, this missing water vapor must be present on the surface. As a minimum, the peak observed value of 1.39 ± 0.47 mg m^{-3} would be expected to extend to the surface producing a layer of density 70 ± 24 mg m^{-2}. However, this layer contains only 40 ± 24 mg m^{-2} of ice indicating that at least 30 ± 24 mg m^{-2} has been deposited on the surface.

[15] This amount of surficial water ice, inferred by observation, is a lower bound as it cannot take into account precipitation of water-ice particles from the fog which may have occurred prior to observation. However, it is possible to quantify this effect by combining the diffusive model with the microphysical model of *Daerden et al.* [2010] to estimate the size of the water-ice fog particles created and to simulate their precipitation to the surface. This diffusive-microphysical model suggests that on sol 113, at the time of measurement, up to 480 mg m^{-2} (0.48 pr-μm) of water ice has already been deposited on the surface from the bottom 50 m of the atmosphere.

[16] As the thickness of the water-ice fog layer simulated in the diffusive-microphysical model grows overnight, more and more water-ice particles may be precipitated towards the surface until mixing and sublimation begin returning this material to the PBL starting after 06:00 LTST the next morning. By that time, the diffusive-microphysical model suggests that the depleted layer will have grown to be of order 260 m thick, and 2.5 pr-μm of water ice will have been deposited on the surface. Thus, the amount of water which is predicted to participate in daily interaction with the surface by the diffusive-microphysical model at this point in the mission represents 6% of the total water column observed on sol 113 of approximately 42 pr- μm [*Tamppari et al.*, 2010].

[17] **Acknowledgments.** This work was enabled by funding from the Canadian Space Agency under contract 9F007-070437/001/SR. The Phoenix mission was led by the University of Arizona, on behalf of NASA, and managed by the Jet Propulsion Laboratory. Paolo D'Odorico thanks two anonymous reviewers.

References

Baran, A. J. (2009), A review of the light scattering properties of cirrus, *J. Quant. Spectrosc. Radiat. Transf.*, *110*(14–16), 1239–1260, doi:10.1016/j.jqsrt.2009.02.026.

Chepfer, H., P. Minnis, D. Young, L. Nguyen, and R. F. Arduini (2002), Estimation of cirrus cloud effective ice crystal shapes using visible reflectances from dual-satellite measurements, *J. Geophys. Res.*, *107*(D23), 4730, doi:10.1029/2000JD000240.

Daerden, F., J. A. Whiteway, R. Davy, C. Verhoeven, L. Komguem, C. Dickinson, P. A. Taylor, and N. Larsen (2010), Simulating observed boundary layer clouds on Mars, *Geophys. Res. Lett.*, *37*, L04203, doi:10.1029/2009GL041523.

Davy, R. (2009) Studies of the Martian boundary-layer, Ph.D. thesis, York Univ., Toronto, Ont., Canada.

Davy, R., J. A. Davis, P. A. Taylor, C. F. Lange, W. Weng, J. Whiteway, and H. P. Gunnlaugson (2010), Initial analysis of air temperature and related data from the Phoenix MET station and their use in estimating turbulent heat fluxes, *J. Geophys. Res.*, *115*, E00E13, doi:10.1029/2009JE003444.

Dickinson, C., J. A. Whiteway, L. Komguem, J. E. Moores, and M. T. Lemmon (2010), Lidar measurements of clouds in the planetary boundary layer on Mars, *Geophys. Res. Lett.*, *37*, L18203, doi:10.1029/2010GL044317.

Hart, H. M., and B. M. Jakosky (1986), Composition and stability of the condensate observed at the Viking Lander 2 site on Mars, *Icarus*, *66*, 134–142, doi:10.1016/0019-1035(86)90013-8.

Lemmon, M. T., et al. (2008), The Phoenix Surface Stereo Imager (SSI) investigation, *Lunar Planet. Sci.*, *XXXIX*, Abstract 2156.

Moores, J. E., M. T. Lemmon, P. H. Smith, L. Komguem, and J. A. Whiteway (2010), Atmospheric dynamics at the Phoenix landing site as seen by the Surface Stereo Imager, *J. Geophys. Res.*, *115*, E00E08, doi:10.1029/2009JE003409.

Smith, P. H., M. T. Lemmon, and C. Shinohara (2007), Phoenix Surface Stereo Imager (SSI) calibration report, *Doc. 415640-1200*, Univ. of Ariz., Tucson.

Smith, P. H., et al. (2009), Water at the Phoenix landing site, *Science*, *325*(5936), doi:10.1126/science.1172339.

Tamppari, L. K., et al. (2010), Phoenix and MRO coordinated atmospheric measurements, *J. Geophys. Res.*, *115*, E00E17, doi:10.1029/2009JE003415.

Whiteway, J., M. Daly, A. Carswell, T. Duck, C. Dickinson, L. Komguem, and C. Cook (2008), Lidar on the Phoenix mission to Mars, *J. Geophys. Res.*, *113*, E00A08, doi:10.1029/2007JE003002.

Whiteway, J., et al. (2009), Mars water ice clouds and precipitation, *Science*, *325*, 68–70, doi:10.1126/science.1172344.

Zent, A. P., M. H. Hecht, D. R. Cobos, S. E. Wood, T. L. Hudson, S. M. Milkovich, L. P. DeFlores, and M. T. Mellon (2010), Initial results from the thermal and electrical conductivity probe (TECP) on Phoenix, *J. Geophys. Res.*, *115*, E00E14, doi:10.1029/2009JE003420.

F. Daerden, Division of Planetary Aeronomy, Belgian Institute for Space Aeronomy, Ringlaan 3, B-1180 Brussels, Belgium. (frank.daerden@aeronomie.be)

C. Dickinson, MacDonald Dettwiler and Associates Space Missions, Brampton, ON L6S 4J3, Canada. (cameron.dickinson@gmail.com)

L. Komguem, J. E. Moores, and J. A. Whiteway, Department of Earth and Space Science and Engineering, York University, Petrie Sciences and Engineering Building, 4700 Keele St., Toronto, ON M3J 1P3, Canada. (komguem@yorku.ca; john.e.moores@gmail.com; whiteway@yorku.ca)

M. T. Lemmon, Atmospheric Sciences Department Texas A&M University, Eller Oceanography-Meteorology Building, College Station, TX 77843-3150, USA. (lemmon@tamu.edu)